Journal of Nanobiotechnology

RESEARCH

Open Access

Tumor specific in situ synthesis of therapeutic agent for precision cancer therapy

Zhixin Zhou[1,2†], Cheng Zhou[1,3†], Jia Liu[1,4,5*], Ye Yuan[3], Chundong Yao[1,2], Miaodeng Liu[1,2,4,5], Lixue Deng[1,2], Jia Sun[1,2], Zuoyu Chen[1,3], Lin Wang[1,2,4,5*] and Zheng Wang[1,3,4,5*]

Abstract

Background Traditional chemotherapeutic agents suffer from a lack of selectivity, poor targeting ability, and drug resistance. Developing tumor-specific therapies is crucial for precisely eliminating tumors while circumventing toxicity to normal tissues. Disulfiram (DSF), an FDA-approved drug for treating alcohol dependence, exhibits antitumor effect by forming complexes with copper ions ($Cu(DDC)_2$). Here, we developed a Cu-doped polydopamine-based nanosystem (DSF@CuPDA-PEGM) to achieve in situ generation of toxic $Cu(DDC)_2$.

Results In cancer cells with elevated H_2O_2 contents, CuPDA responsively degrades to release Cu ions and DSF, allowing on-site synthesis of $Cu(DDC)_2$ with potent antitumor activity. DSF@CuPDA-PEGM exhibits excellent therapeutic efficacy against both drug-sensitive and drug-resistant cancer cells while minimizing toxicity to noncancerous cells. Moreover, DSF@CuPDA-PEGM promotes the immune response by inducing cancer cell immunogenic death, thereby augmenting anti-PD-1-based immune checkpoint blockade therapy.

Conclusion A tumor-specifically degradable Cu-doped polydopamine-based nanosystem is developed to achieve in situ synthesis of antitumor compounds, providing a promising approach to precisely eliminate tumors and heighten chemo-immunotherapy.

Keywords Cancer therapy, Disulfiram, Tumor microenvironment, In situ synthesis of antitumor agent, Nanomedicine

†Zhixin Zhou and Cheng Zhou contributed equally to this work.

*Correspondence:
Jia Liu
jialiu1207@hust.edu.cn
Lin Wang
lin_wang@hust.edu.cn
Zheng Wang
zhengwang@hust.edu.cn

Full list of author information is available at the end of the article

Graphical Abstract

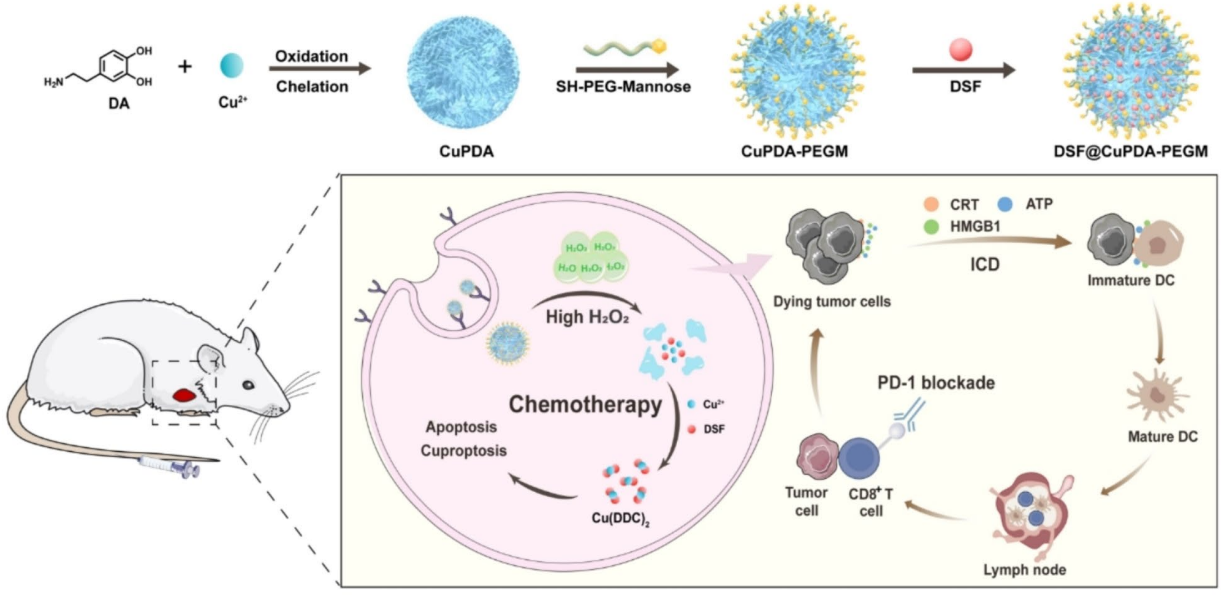

Introduction

Colorectal cancer (CRC) is the third most commonly occurring tumor with high morbidity and mortality [1]. Chemotherapy stands as a primary strategy in the treatment of CRC, especially for patients with unresectable disease lesions. However, current chemotherapeutic drugs (e.g., fluorouracil and oxaliplatin) cause unfavorable and inevitable damage to healthy tissues due to the nonspecific toxicity and poor targeting ability, and critically suffer from cancer drug resistance, resulting in limited therapeutic efficacy and serious side effects [2]. Hence, there is an urgent need to develop tumor-specific therapeutic agents or strategies for precisely eradicating colorectal tumors, which are able to conceal their toxicity in normal tissues and unleash the antitumor effects in tumors for eliminating both drug-sensitive and resistant cancer cells.

Disulfiram (DSF), a clinical drug used for treating alcoholism, has recently been demonstrated to possess anticancer properties [3]. DSF itself exhibits low toxicity, but its interaction with copper ions leads to the formation of toxic $Cu(DDC)_2$ (Scheme 1) [4]. The formed complex binds with NPL4 and disables the p97-NPL4-UFD1 pathway, consequently inducing cell apoptosis [5]. Hence, the cell-killing effects of DSF are highly dependent on the copper ions, conferring DSF with selectivity on toxification. To enhance the DSF-based chemotherapy, a variety of DSF/Cu^{2+} co-delivering nanosystems have been developed, which promote the accumulation in tumors and release Cu^{2+} triggered by acidic conditions after cellular internalization for the generation of $Cu(DDC)_2$ [6–12]. However, these nanosystems could also release Cu ions in the acidic endo/lysosomes in noncancerous cells to allow chelation of Cu^{2+}/DSF, causing potential toxicity to normal tissues. Moreover, Cu^{2+} leakage will facilitate the generation of reactive oxygen species (ROS) owing to the Cu-catalyzed Fenton-like reactions, inducing cellular oxidative stress and non-specific toxicity [13]. Thus, an ideal DSF-based therapeutic system requires the specific release of Cu^{2+} inside tumor tissues or cells, allowing in situ synthesis of $Cu(DDC)_2$ for precisely eradicating tumors.

Reactive oxygen species (ROS) comprise a wide variety of reactive chemical species of oxygen metabolites that play a crucial role in regulating cellular function [14]. Cancer cells live in an aberrant redox homeostasis [15]. The hyperproliferation and active metabolism of cancer cells cause the overproduction of ROS, and cancer cells increase their antioxidant systems to maintain the redox balance [16]. Compared with normal cells and tissues, the levels of hydrogen peroxide (H_2O_2) in tumor cells and microenvironment are significantly elevated (~ 100 μM) [17]. Of note, the H_2O_2 contents in drug-resistant cancer cells are even higher than those in drug-sensitive parent cancer cells [18, 19]. The distinct difference in H_2O_2 levels between tumors and normal tissues might be a promising key for designing therapeutic nanosystems for precise tumor elimination. Notably, the $Cu(DDC)_2$ complex has been demonstrated to facilitate the generation of cellular ROS, thereby elevating H_2O_2 levels [20]. Thus, we

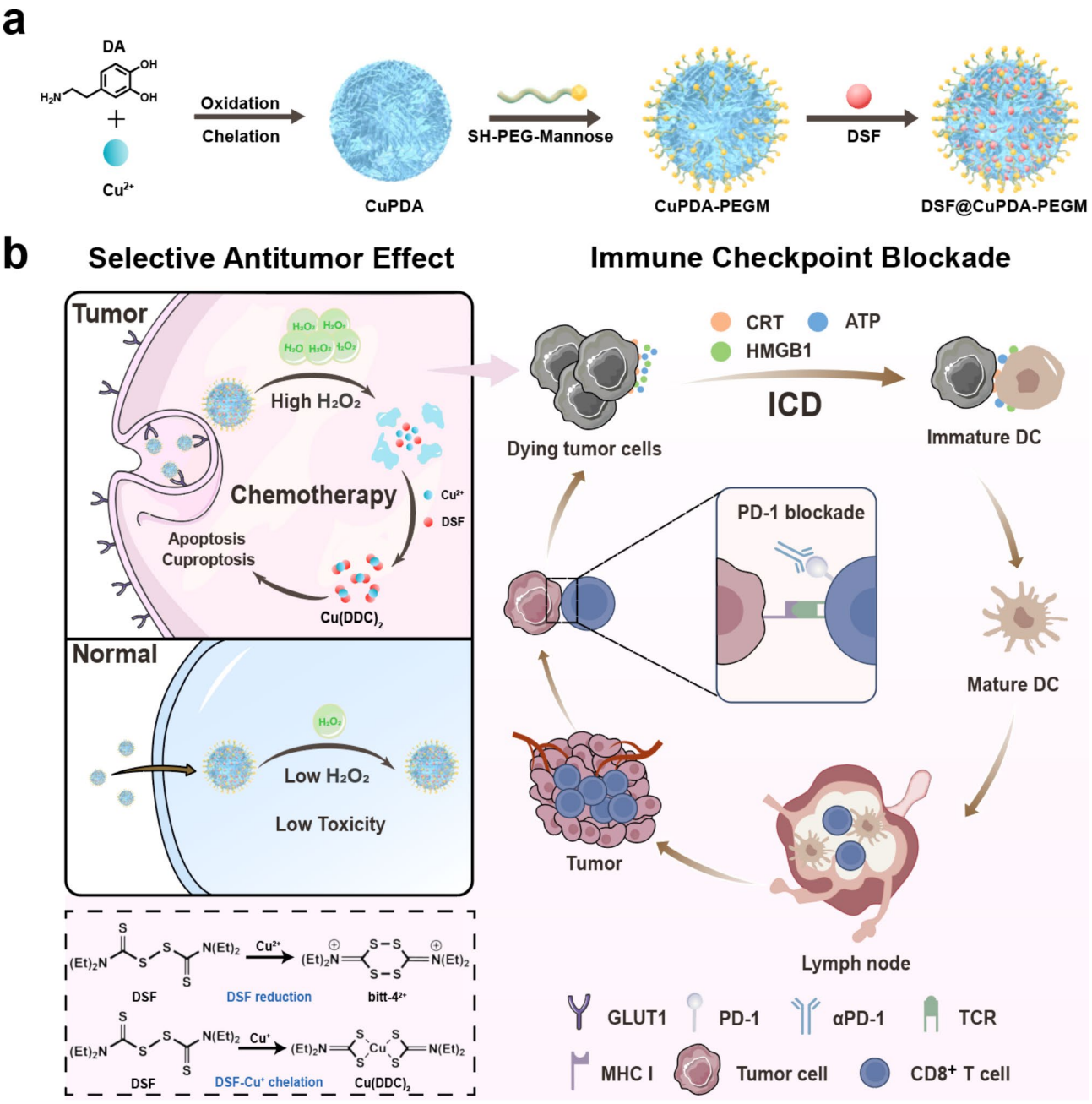

Scheme 1 A scheme illustration on the preparation (**a**) and precise tumor therapy (**b**) of CuPDA-based nanosystem

hypothesized that an H_2O_2-responsive copper-containing nanosystem would selectively unload the Cu ions and DSF, enabling in situ synthesis of $Cu(DDC)_2$ in tumors with high levels of H_2O_2. Furthermore, the synthesized $Cu(DDC)_2$ promotes H_2O_2 production intracellularly, which would cyclically trigger the release of Cu^{2+} and the synthesis of $Cu(DDC)_2$. This therapeutic approach will achieve precise tumor elimination and help to minimize the toxicity to normal tissues. More importantly, the elevated levels of H_2O_2 in drug-resistant cancer cells might promote the synthesis of $Cu(DDC)_2$, inducing enhanced antitumor effects for overcoming drug resistance.

Polydopamine (PDA) is a melanin-like synthetic polymer derived from dopamine, a naturally existing substance in the human body [21]. PDA nanoparticles are regarded as an exceptional material for drug delivery owing to their good biocompatibility and minimal long-term toxicity, as well as the presence of cavities and surfaces that enable efficient drug loading [22]. Interestingly, PDA and its derivatives could effectively scavenge multiple types of ROS to protect tissues from

oxidative stress-related injury and could be simultaneously degraded by the reactive species (e.g., H_2O_2) [23]. Moreover, PDA possesses excellent chelation capability of metal ions due to the abundant catechol and amino groups [24, 25]. Based on the versatile characteristics of PDA, it would be a feasible strategy to design a copper-embedded PDA derivative that allows controllable Cu^{2+} release and in situ coordination with DSF in response to the high levels of H_2O_2 within tumor tissues or cells.

Herein, we have synthesized copper ion-doped polydopamine nanoparticles (CuPDA) through oxidation polymerization and Cu-chelation, which were subsequently modified with mannose-terminated polyethylene glycol (PEG-Mannose) to enhance the colloidal stability and tumor targeting ability (Scheme 1). In the presence of H_2O_2, CuPDA responsively degrades to free Cu ions, allowing the formation of $Cu(DDC)_2$ complexes with excellent antitumor activity. Notably, the CuPDA-based nanosystem (DSF@CuPDA-PEGM) could selectively kill colorectal cancer cells, particularly demonstrating great antitumor effects against drug-resistant cancer cells, but exhibiting low toxicity towards noncancerous cells. Moreover, DSF@CuPDA-PEGM could induce immunogenic cell death (ICD) to stimulate the antitumor immune response, thereby enhancing the immune checkpoint therapy against the microsatellite stable (MSS) CRC tumor. Thus, this CuPDA-based nanosystem offers an effective and precise strategy against CRC tumors and provides a new insight for chemo-immunotherapy.

Materials and methods

Materials

Dopamine hydrochloride, disulfiram, rhodamine123, phloretin, and *N*-acetyl-L-cysteine were obtained from Aladdin Industrial Corporation (Shanghai, China). Hydrogen peroxide (30%), ethanol (AR, ≥95%), and ammonia solution (AR, 25–28%) were purchased from Sinopharm Chemical Regent Co., Ltd (Shanghai, China). SH-PEG-Mannose (Mn, 5000 Da) was purchased from Huateng Pharma (Hunan, China). 2′,7′-Dichlorofluorescin diacetate (DCFH-DA), calcein acetoxymethyl ester (Calcein-AM), propidium iodide (PI), and Enhanced ATP Assay Kit were purchased from Beyotime Chemical Reagent (Jiangsu, China). Lysotracker was purchased from Yeasen Biotech Co., Ltd (Shanghai, China). HMGB1 antibody and goat anti-Mouse lgG AF 488 were provided by Abmart Co., Ltd (Shanghai, China). Antibodies for flow cytometry were purchased from Biolegend, lnc (USA). In Vivo MAb anti-mouse PD-1 (CD279) was obtained from BioXcell (USA).

Preparation of DSF@CuPDA-PEGM

CuPDA nanoparticles were prepared through the oxidative polymerization and self-assembly of dopamine (DA) with Cu^{2+} chelation under the alkaline condition. Firstly, dopamine hydrochloride (380 mg, 2 mmol) and $CuCl_2{\cdot}2H_2O$ (28.4 mg, 0.17 mmol) were dissolved in 10 mL of deionized water, respectively. Then, dopamine hydrochloride and $CuCl_2{\cdot}H_2O$ solutions were added into a mixture of ammonium hydroxide (3 mL), ethanol (40 mL), and deionized water (90 mL) at room temperature stirring for 24 h. CuPDA nanoparticles were collected by centrifuging, washing, and freeze-drying.

SH-PEG-Mannose (5k) was modified to the surface of the CuPDA nanoparticles. Firstly, CuPDA NPs (20 mg) were dispersed in 20 mL of Tris buffer (10 mM, pH 8.5) containing SH-PEG-Mannose (20 mg). The reaction carried on at room temperature for 24 h and CuPDA–PEGM was collected via centrifugation and washing.

To encapsulate the hydrophobic DSF, CuPDA-PEGM (20 mg) was dispersed in ethanol solution (10 mL) with DSF (10 mg) and stirred at room temperature for 24 h. The resulting DSF@CuPDA-PEGM was collected by centrifugation and washing with ethanol and water.

Characterization of DSF@CuPDA-PEGM

A JEM-2010 F transmission electron microscope (TEM, JEOL, Japan) was employed for morphological characterization of nanoparticles. Element mapping was conducted on FEI-Talos F200S. X-ray photoelectron spectroscopy (XPS) spectra were obtained by ESCALAB 250Xi (Thermo Fischer). The hydrodynamic size and zeta potential of nanoparticles were measured by the Zetasizer Nano series (Nano-ZS ZEN3600, Malvern). UV-Vis absorption spectra were observed on a VICTOR Nivo Multimode Microplate Reader (PerkinElmer). CuPDA-PEGM NPs were incubated in PBS or DMEM with 10% FBS for 1 h and 24 h to investigate their stability, then the hydrodynamic sizes were measured.

Hydrogen peroxide-responsive degradation and copper ion release in vitro

CuPDA NPs (0.25 mg/mL) were incubated with different amounts of H_2O_2 (0, 0.1, 1, 5, 10 mM) in aqueous solutions. After 72 h, UV-vis absorption spectra of solutions from 400 to 800 nm were measured. Cu^{2+} concentrations in supernatants were investigated by Inductively coupled plasma atomic emission spectrometer (ICP-AES). For different incubation times (6, 12, 24, 48, 72 h), the absorbance of CuPDA NPs at 500 nm was recorded.

To study the degradation behaviors, DSF@CuPDA-PEGM dispersions were incubated in the buffers mimicking different environments (pH 5.0 with 100 μM H_2O_2, pH 6.5 with 100 μM H_2O_2, and pH 7.4 with 3.6 μM H_2O_2) over 72 h. After incubation (6, 12, 24, 48, 72 h), the absorbance of DSF@CuPDA-PEGM dispersion at 500 nm was recorded. To test DSF release, DSF@CuPDA-PEGM (2 mg of DSF) was dispersed in the buffers (pH 7.4, 3.6

μM H_2O_2 or pH 6.5, 100 μM H_2O_2), and then dialyzed in 10 mL of corresponding buffers. At given time intervals, the release media were collected and replaced with fresh buffers. The amount of released DSF was evaluated and calculated according to the reported method [26].

In vitro cellular uptake

Rhodamine123 was loaded on CuPDA-PEG or CuPDA-PEGM to explore in vitro cellular uptake. For Rh123@CuPDA-PEG and Rh123@CuPDA-PEGM synthesis, 3 mg Rhodamine123 was dissolved in 500 μL ethanol, which was later added into CuPDA-PEG or CuPDA-PEGM suspensions (10 mg/mL). After stirring overnight, Rh123@CuPDA-PEG and Rh123@CuPDA-PEGM were dialyzed in water for two days and freeze-dried for use.

To investigate GLUT1-mediated cellular uptake, HCT116 cells were seeded in confocal dishes (5×10^4 cells/well). After 24 h, cell media were replaced with fresh media containing Rh123@CuPDA-PEG or Rh123@CuPDA-PEGM (1.25 μg/mL). For the phloretin inhibition group, the cells were pretreated with phloretin for 12 h before exposure to Rh123@CuPDA-PEGM. For the mannose competition group, the cells were exposure to Rh123@CuPDA-PEGM in the media containing mannose (4.5 g/L) for 4 h. After treatment for 4 h, the cells were stained with Hoechst 33,342, and then observed on a confocal. For flow cytometry analysis, HCT116 cells (2×10^5 cells per well) were cultured in a 6-well plate for 24 h, and treated as mentioned above before flow cytometry analysis.

In vitro cytotoxicity and apoptosis assay

HCT116, HUVEC, L929, CT26, NCM460, and 3T3 cells were seeded in the DMEM medium with 10% fetal bovine serum (FBS) at 37 °C in an incubator with 5% CO_2. HCT116 L/OHP cells were cultured in RPMI-1640 medium with 10% FBS at 37 °C under the atmosphere of 5% CO_2.

The cytotoxicity of different drug formulations (DSF, CuPDA-PEGM, DSF@CuPDA-PEG, DSF@CuPDA-PEGM) towards HCT116 cells, HCT116 L/OHP cells, HUVEC cells, L929 cells, Hela cells, MCF-7 cells and A549 cells were measured by a CCK-8 kit (Vazyme). Briefly, cells (6×10^3 cells per well) were cultured in 96-well plates for 24 h. Then, the cell culture media were replaced with media containing different formulations (0–5 μg/mL DSF, 0–50 μg/mL CuPDA-PEGM). After incubating for 24 h, the cell viability was evaluated by a CCK-8 assay according to the manufacturer's instructions.

Cell apoptosis assay was conducted through an Annexin V/PI kit. First, HCT116 or HUVEC cells (2×10^5 cells per well) were cultured in a 6-well plate for 24 h. DSF (2.5 μg/mL), CuPDA-PEGM (25 μg/mL), DSF@CuPDA-PEG (2.5 μg/mL DSF), DSF@CuPDA-PEGM (2.5 μg/mL DSF) were applied to treat these cells. After 24 h, the cells were washed, collected, and stained with Annexin V and PI for flow cytometry analysis.

For live/dead staining, HCT116 or HUVEC cells (1×10^5 cells per well) were cultured in a 12-well plate and incubated for 24 h. The cells were treated as mentioned above. After that, the media were discarded and the cells were stained with Calcein-AM and PI for 30 min before observation by a fluorescence microscope.

The mechanisms of in vitro cell cytotoxicity

For intracellular ROS levels detection, HCT116 cells (1×10^5 cells per well) were seeded in a 12-well plate and incubated for 24 h, followed by treatment with DSF@CuPDA-PEGM (1.25 μg/mL) for different times (1 h, 2 h, 4 h, 8 h, 24 h). DCFH-DA probe (10 μM) was used to indicate the cellular ROS of the treated cells.

To alter the ROS content in HCT116 cells, H_2O_2 and *N*-acetyl-L-cysteine (NAC) were applied. HCT116 cells (1×10^5 cells per well) were seeded in a 12-well plate and incubated overnight. Then the culture media were replaced with fresh medium containing 0.2 mM H_2O_2 or 0.5 mM NAC and incubated for 4 h. Afterward, the cells were treated with serum-free media containing DCFH-DA (10 μM) and incubated for 20 min before imaging using a fluorescence microscope. For flow cytometry analysis, HCT116 cells (2×10^5 cells per well) were cultured in a 6-well plate overnight. Cells were treated with the same procedure as mentioned above, and then the cells were collected for flow cytometry analysis.

To investigate the impact of intracellular ROS on DSF@CuPDA-PEGM's selective killing ability, cells (6×10^3 cells per well) cultured in a 96-well plate were pretreated with 0.2 mM H_2O_2 or 0.1 mM NAC, then cells were incubated with DSF@CuPDA-PEGM (DSF, 0–5 μg/mL) for 24 h. Afterward, the cell viability was measured by a CCK-8 assay.

In order to explore the cell death mechanisms induced by DSF@CuPDA-PEGM, HCT116 cells were pretreated with Z-VAD-FMK (30 μM) or rotenone (100 nM), and then exposed to DSF@CuPDA-PEGM (DSF, 0–5 μg/mL). After incubation for 24 h, the cell viability was evaluated by a CCK-8 assay.

In vitro ICD effect

To assess the ICD effect of DSF@CuPDA-PEGM, ICD-related DAMPs (HMGB1 and ATP) were evaluated in CT26 cells in vitro. CT26 cells were treated with free DSF, CuPDA-PEGM, DSF@CuPDA-PEG, and DSF@CuPDA-PEGM (2.5 μg/mL of DSF), respectively. After 4 h, the cells were washed, fixed, and stained with anti-HMGB1 primary antibody, followed by Alexa Fluor 488

secondary antibody according to the manufacturer's protocol.

After CT26 cells were incubated with these drug formulations for 5 h, the media were collected and centrifuged at 1000 rpm for 5 min. ATP contents in the supernatants were tested using an Enhanced ATP Assay Kit according to the manufacturer's instructions.

To evaluate DCs maturation, the culture media of CT26 cells were collected and centrifuged after treatment with free DSF, CuPDA-PEGM, DSF@CuPDA-PEG, and DSF@CuPDA-PEGM for 24 h. Then, DC2.4 cells were treated with these condition media for 24 h. Finally, the DCs were collected and stained with anti-CD11c-BV421 and anti-CD86-PE antibodies. The proportion of mature DCs was determined by flow cytometry.

Animals

Female BALB/c nude mice (6 weeks) were obtained from Beijing Vital River Laboratory Animal Technology Co., Ltd. (Beijing, China). Female BALB/c mice (6–8 weeks) were provided by Liaoning Changsheng Biotechnology Co., Ltd. (Benxin, China). All animal experiments were performed according to the protocols approved by the Animal Care and Use Committee of Huazhong University of Science and Technology (Wuhan, China).

In vivo antitumor effect

To evaluate the in vivo therapeutic effects of DSF@CuPDA-PEGM, subcutaneous HCT116 tumor-bearing models in BALB/c nude mice were used. HCT116 cells (1.2×10^6 cells) were injected into the right infra-axillary dermis subcutaneously to develop models. Tumor-bearing mice were randomly divided into 5 groups ($n=6$): (1) PBS control, (2) free DSF, (3) CuPDA-PEGM, (4) DSF@CuPDA-PEG, (5) DSF@CuPDA-PEGM. The mice were intravenously injected with 200 μL of the above formulations every three days for 4 times since the tumor volume reached approximately 100 mm^3. The dosages of DSF and CuPDA-PEGM were 3.75 mg/kg and 37.5 mg/kg, respectively. Body weight and tumor volume were monitored every two days. Tumor volume was calculated according to the following formula: $V=1/2\times width^2\times length$. Mice were sacrificed at day 18, major organs were collected and stained with hematoxylin and eosin, while the tumors were weighed and performed with TdT-mediated dUTP nick-end labeling (TUNEL) staining.

In vitro biocompatibility

Hemolysis assay was performed to evaluate the biocompatibility of CuPDA-PEGM. Red blood cells suspension (900 μL, 2%) was incubated with 100 μL CuPDA-PEGM (0–100 μg/mL) under vibration for 4 h at 37 °C. Then, the mixtures were centrifuged at 3000 rpm for 10 min and the supernatants were measured at 545 nm. PBS and Triton X-100 were applied as the negative and positive controls.

The cytotoxicity of CuPDA-PEGM NPs (0–100 μg/mL) in noncancerous cell lines (L929, NCM460, and 3T3) was evaluated by a CCK-8 kit according to the methods mentioned above.

In vivo antitumor efficacy by DSF@CuPDA-PEGM/αPD-1 combination

When CT26 tumor volumes reached around 80 mm^3, mice were treated with PBS, αPD-1, DSF@CuPDA-PEGM, DSF@CuPDA-PEGM/αPD-1, respectively ($n=6$, 3.75 mg/kg of DSF, 100 μg of αPD-1 per mouse). The body weight and tumor volumes of mice were monitored every day. On day 12, mice were sacrificed and their tumors were harvested for staining with CD8 antibody. Cells with red fluorescence around blue nuclei were regarded as $CD8^+$ T cells.

To investigate the immune responses of mice, CT26 tumor-bearing BALB/c mice were divided into 4 groups randomly ($n=4$). DSF@CuPDA-PEGM (DSF: 3.75 mg/kg) were intravenously injected two times on day 0 and day 3, and αPD-1 was intraperitoneally administered on day 1 and day 4 at a dose of 100 μg/mouse. Mice were sacrificed on day 5. Their tumors and tumor-draining lymph nodes were collected for flow cytometry analysis. The tumors were pulverized and the collected cells were washed with 1640 medium followed by staining with specific antibodies including CD4-BV605, and CD8a-APC. The lymph nodes were obtained and collected for CD11c-FITC and CD86-PE staining. The cells were finally analyzed by flow cytometry.

Results and discussion

Preparation and characterization of DSF@CuPDA-PEGM

The copper ion-doped polydopamine (CuPDA) was synthesized through oxidative polymerization and $Cu^{(II)}$-doping in the alkaline condition at room temperature. During the oxidation and crosslinking of dopamine, the Cu^{2+} would be embedded in the polymeric nanoparticles through coordination with catechol, carboxy, and imine groups. The CuPDA exhibited a spherical shape with an average diameter of 180 nm (Fig. 1a), similar to that of PDA nanoparticles (Fig. S1a), suggesting that the copper incorporation would not change the morphology of polydopamine. The element mapping visually revealed that the Cu, O, C, and N elements were homogeneously distributed in the CuPDA nanoparticles (Fig. 1b), indicating the successful chelation of Cu ions during dopamine polymerization. The Cu content in CuPDA was examined to be 1.92% by inductively coupled plasma atomic emission spectrometer (ICP-AES). Next, the Cu coordination status within CuPDA was analyzed by X-ray photoelectron spectroscopy (XPS) (Fig. 1c). The Cu 2p spectrum

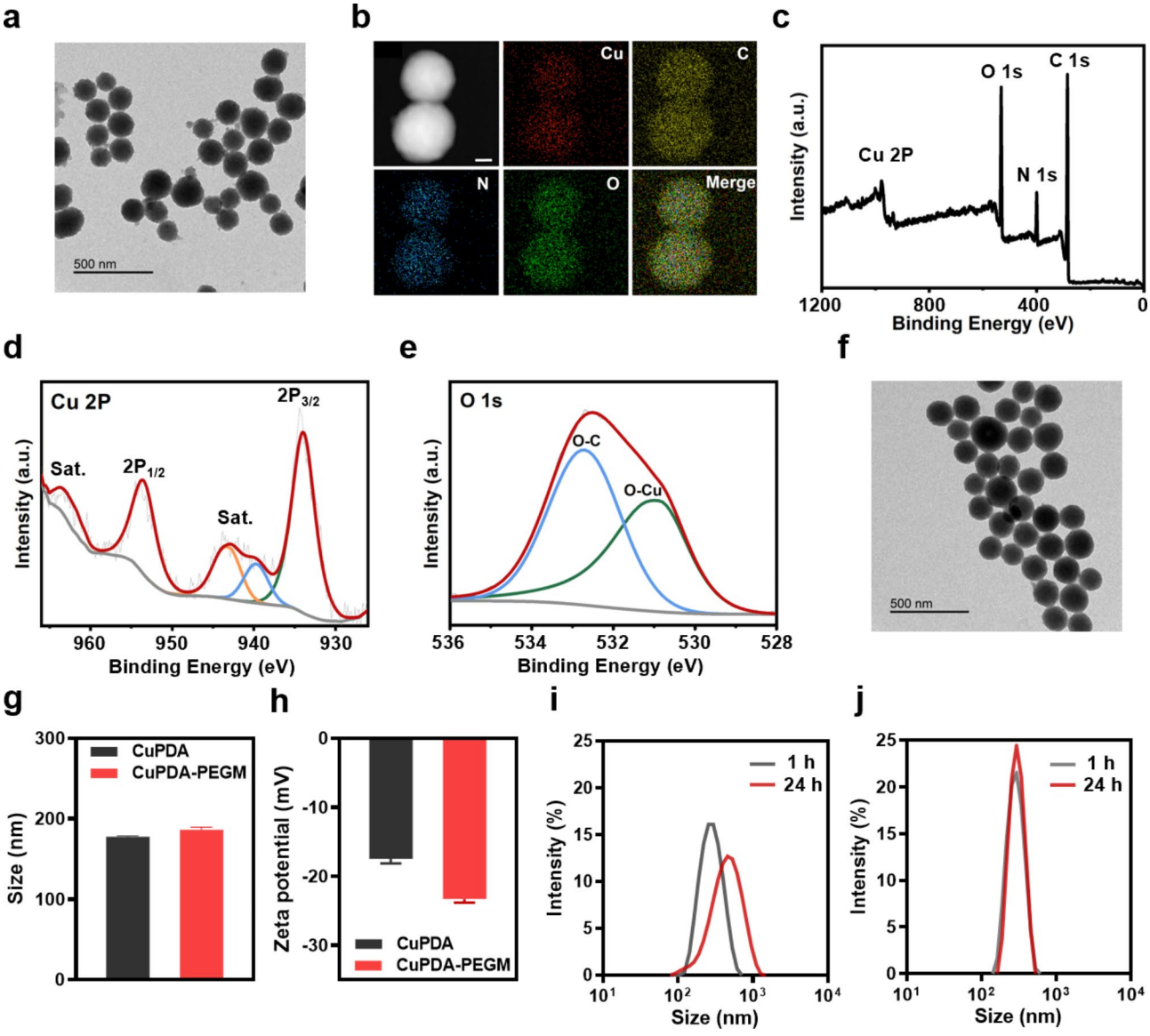

Fig. 1 Characterization of DSF@CuPDA-PEGM. (**a**) TEM image of CuPDA. Scale bar, 500 nm. (**b**) Element mapping of CuPDA. Scale bar, 50 nm. (**c**) XPS survey spectrum of CuPDA. (**d, e**) Cu 2P XPS spectrum (**d**) and O 1s XPS spectrum (**e**) of CuPDA. (**f**) TEM image of CuPDA-PEGM. Scale bar, 500 nm. (**g**) Hydrodynamic sizes of CuPDA and CuPDA-PEGM. (**h**) Zeta potential of CuPDA and CuPDA-PEGM. (**i, j**) The size distribution of CuPDA-PEGM dispersions in PBS (**i**) or DMEM containing 10% FBS (**j**) after incubation for 1 h and 24 h

exhibited two characteristic peaks at 934 eV (Cu $2p_{3/2}$) and 953.7 eV (Cu $2p_{1/2}$) along with two satellite peaks (Fig. 1d), indicating the existence of $Cu^{(II)}$. In the O 1s spectrum (Fig. 1e), the peaks at 532.7 eV and 531.0 eV were attributed to O–C and O-Cu, respectively, confirming the Cu coordination in CuPDA.

To endow the CuPDA nanoparticles with tumor-targeting capability and colloidal stability, mannose-terminated polyethylene glycol (SH-PEG-Mannose, Mn: 5000 Da) was decorated on the surface of CuPDA by the Michael addition reaction between the thiol group of SH-PEG-Mannose and quinone on CuPDA [21]. After modification of PEG-Mannose, the morphology of nanoparticles remained spherical (Fig. 1f), while the hydrodynamic size increased by 8.7 nm and the zeta-potential decreased by 5.8 mV (Fig. 1g and h). Fourier transform infrared (FTIR) spectrum of CuPDA-PEGM revealed the aliphatic C–H stretching in PEG (~2880 cm^{-1}), suggesting the successful modification of SH-PEG-Mannose (Fig. S1b). Of note, the PEG-Mannose coating significantly enhanced the colloidal stability of nanoparticles, as the particle sizes of CuPDA-PEGM in physiological buffers (PBS and cell medium) hardly changed after incubation for 24 h (Fig. 1i and j). Finally, DSF was loaded in CuPDA-PEGM through hydrophobic interactions with a loading content of 8.4%. Meanwhile, the SH-PEG-modified CuPDA

(CuPDA-PEG) was synthesized as the control without targeting moiety.

Hydrogen peroxide (H_2O_2)-responsive degradation and copper ion release

It was reported that PDA could undergo oxidation-induced degradation in the presence of reactive oxygen species (ROS), such as H_2O_2 [22]. Herein, we investigated whether Cu-chelated PDA could degrade and release Cu ions in the presence of H_2O_2. CuPDA nanoparticles were exposed to H_2O_2 aqueous solutions at different concentrations for 72 h. Upon incubation with H_2O_2 solution, the color of CuPDA suspensions faded in a dose-dependent manner and became light brown after incubation with 10 mM H_2O_2 (Fig. 2a). TEM images exhibited the morphological changes of H_2O_2-treated CuPDA, suggesting the degradation of CuPDA (Fig. S2). The UV-Vis spectra further confirmed the degradation of CuPDA in H_2O_2 solution, as the absorption of CuPDA suspensions (from 400 nm to 800 nm) decreased with increasing H_2O_2 concentration and incubation time (Fig. 2b and c). Reasonably, CuPDA responsively released Cu ions due to the degradation induced by H_2O_2, while only 6% of Cu^{2+} were leaked from CuPDA in the physiological condition without H_2O_2 (Fig. 2d). Moreover, the degradation behaviors of DSF@CuPDA-PEGM were examined in the buffers mimicking different environments (Fig. S3). Of note, high levels of H_2O_2 and acidic environment

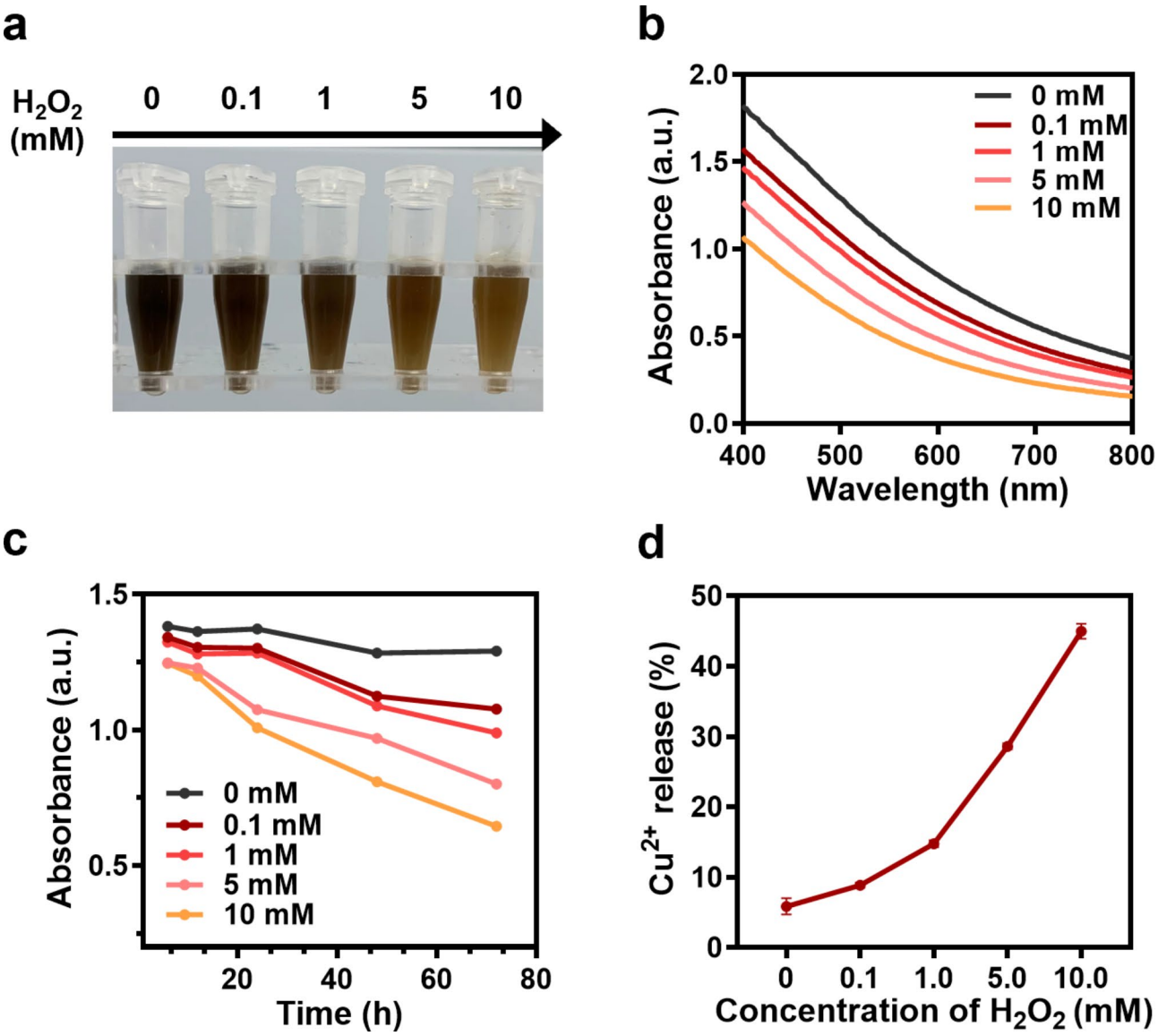

Fig. 2 Hydrogen peroxide-responsive degradation. (**a**) Image of CuPDA incubated in H_2O_2 solutions at different concentrations for 72 h. (**b**) UV-Vis absorption spectra of CuPDA after incubation with H_2O_2 for 72 h. (**c**) Relative absorbance of CuPDA dispersions at 500 nm in the H_2O_2 solution over 72 h. (**d**) Cu ion release amounts from CuPDA in the H_2O_2 solutions at different concentrations at 72 h

significantly accelerated the degradation rate of nanoparticles and promoted the DSF release (Fig. S3 and S4). These results indicate that CuPDA would specifically release Cu ions and DSF in response to the tumor microenvironment with high contents of H_2O_2 (~100 μM) [17], which might further generate cytotoxic $Cu(DDC)_2$ for precision cancer therapy. On the contrary, the Cu ions would be restricted in the nanoparticles to avoid side effects in normal tissues or cells with low contents of H_2O_2.

Cellular internalization of CuPDA-PEGM in vitro

The glucose transporter type 1 (GLUT1) has been identified to be over-expressed on the membranes of colorectal cancer cells (CRC) [27, 28], and relatively low expressed in the immune cells [29], which is a potential target for drug delivery for CRC. Thus, mannose ligands (the epimer of glucose that could specifically bind to GLUT1 [30]) were modified on the surface of CuPDA (CuPDA-PEGM) to endow it with targeting capability to enhance the drug delivery efficacy. To test this notion, Rhodamine 123 (Rh123, green fluorescence) was loaded in CuPDA-PEGM for the visualization of endocytosis behaviors. The CuPDA modified with SH-PEG (without mannose ligand) was synthesized as a control. After co-incubation with HCT116 cells for 4 h, more green fluorescent spots could be observed in the cells exposed to Rh123@CuPDA-PEGM compared with the cells incubated with Rh123@CuPDA-PEG (Fig. 3a), suggesting that more Rh123@CuPDA-PEGM was internalized in HCT116 cells. Moreover, the phloretin (a GLUT1 inhibitor) significantly weakened the cellular uptake of Rh123@CuPDA-PEGM, indicating that the enhanced internalization was dependent on the GLUT1/mannose-mediated targeting effect. Furthermore, the flow cytometry analysis confirmed the targeting effect of CuPDA-PEGM in GLUT1-positive cancer cells when the cells were pretreated with either mannose or phloretin (Fig. 3b and Fig. S5). In addition, the internalized Rh123@CuPDA-PEGM was mainly observed in the cytoplasm and highly overlapped with the lysosomes (Fig. S6). These results suggest that the mannose decoration promotes the cellular uptake efficacy of CuPDA-PEGM in colorectal cancer cells with overexpressed GLUT1.

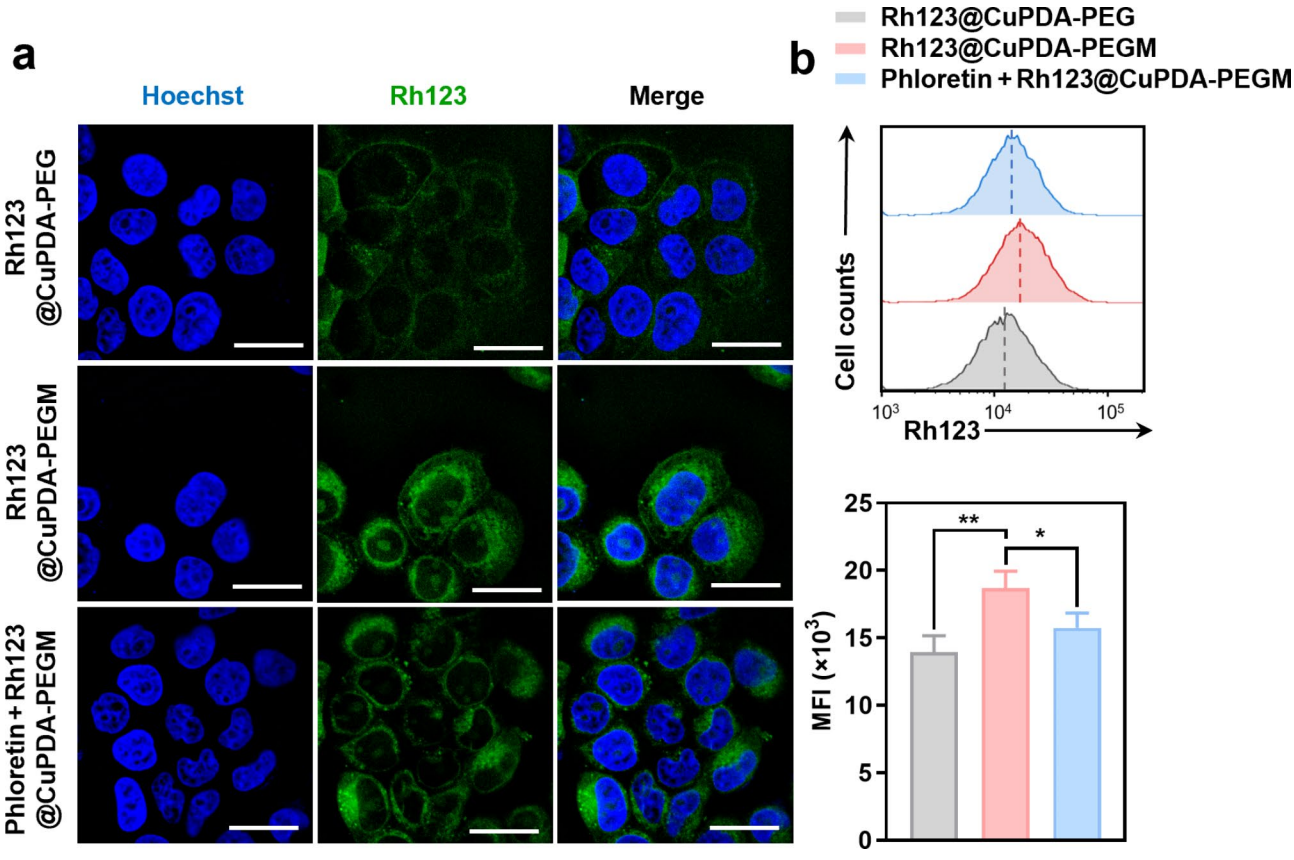

Fig. 3 Cellular internalization of CuPDA-PEGM in vitro. (**a**) Confocal images of HCT116 cells exposed to Rh123@CuPDA-PEG, Rh123@CuPDA-PEGM, or Rh123@CuPDA-PEGM with phloretin-pretreatment. Scale bars, 20 μm. (**b**) Flow cytometry analysis (upper) and mean fluorescence intensity (MFI) (lower) of HCT116 cells treated with Rh123@CuPDA-PEG, Rh123@CuPDA-PEGM, or Rh123@CuPDA-PEGM with phloretin-pretreatment

Specific antitumor effect of DSF@CuPDA-PEGM in vitro

To study the antitumor effect of DSF-loaded CuPDA-PEGM, the cytotoxicity of different formulations against colorectal cancer cells and noncancerous cells was investigated by CCK-8 assay. Of note, in the drug-sensitive cancer cells (HCT116, human colorectal cancer cells) and drug-resistant cancer cells (HCT116/L-OHP, an oxaliplatin-resistant counterpart), DSF@CuPDA-PEG and DSF@CuPDA-PEGM exhibited dose-dependent cytotoxicity, while DSF alone barely killed the cancer cells (Fig. 4a and b). Owing to the targeting ability of mannose, DSF@CuPDA-PEGM showed an enhanced antitumor effect compared with DSF@CuPDA-PEG. Impressively, both DSF@CuPDA-PEG and DSF@CuPDA-PEGM exhibited greater antitumor effects against the drug-resistant cancer cells, as the IC_{50} of these formulations decreased by ~36% in HCT116/L-OHP cells compared to HCT116 cells (Table S1). Moreover, in other types of cancer cells, DSF@CuPDA-PEGM also exhibited effective antitumor effects (Fig. S7). In sharp contrast, the cytotoxicity of both DSF@CuPDA-PEG and DSF@CuPDA-PEGM in noncancerous cells (HUVEC and L929) was markedly lower than that in cancer cells (Fig. 4c and d), suggesting the specific antitumor effects. Next, the apoptosis assay and live/dead staining images revealed that DSF@CuPDA-PEG and DSF@CuPDA-PEGM could precisely induce cell death in HCT116 cells, but hardly reduced the viability of HUVEC cells (Fig. 4e-h). Of note, DSF@CuPDA-PEGM induced more apoptotic cells or PI-positive cells in these assays compared with DSF@CuPDA-PEG (Fig. 4e and g), confirming that the mannose-GLUT1 mediated targeting effect enhances the antitumor activity. These results consistently demonstrate that the CuPDA-based nanosystems (CuPDA-PEG and CuPDA-PEGM) are capable of delivering DSF to selectively kill cancer cells while exhibiting minimal toxicity toward noncancerous or normal cells. In addition, the mannose functionalization could further enhance the antitumor effect of DSF@CuPDA-PEGM in the GLUT1-positive cancer cells.

DSF@CuPDA-PEGM exhibits the specific antitumor effect depending on the cellular ROS and induces immunogenic cell death

Hydrogen peroxide is considered as the major source of cellular ROS and has a relatively long biological lifespan [31–33]. Given that CuPDA could degrade and release Cu ions in response to H_2O_2, which will chelate with DSF to synthesize the antitumor agent, the cytotoxicity of DSF@CuPDA-PEGM may be dependent on the intracellular ROS levels that trigger CuPDA degradation for in situ $Cu(DDC)_2$ synthesis. To test this notion, the intracellular ROS level of HCT116 cells was monitored after exposure to DSF@CuPDA-PEGM (DSF: 1.25 μg/mL, with low cytotoxicity) for 24 h (Fig. 5a and b, Fig. S8). The ROS levels (indicated by the green fluorescence of DCF) of HCT116 cells were gradually decreased over time, and the mean fluorescence intensity reduced to 37% at 24 h post-treatment, suggesting that DSF@CuPDA-PEGM consumes the ROS intracellularly and may release Cu ions responsively. Next, H_2O_2 and *N*-acetyl-L-cysteine (NAC) were employed to upregulate and downregulate the cellular ROS contents in HCT116 cells, respectively. H_2O_2 pretreatment markedly increased the intracellular ROS level (Fig. 5c and d, Fig. S9a), which enhanced the antitumor effect of DSF@CuPDA-PEGM (Fig. 5e). In contrast, NAC pretreatment significantly reduced the intracellular ROS content (Fig. 5c and d, Fig. S9a), which suppressed the cytotoxicity of DSF@CuPDA-PEGM (Fig. 5f). As a precursor of reduced glutathione (GSH), NAC pretreatment could increase the intracellular GSH, which could chelate with Cu ions to form Cu-GSH complexes. Since Cu-GSH complexes could be disassembled to form $Cu(DDC)_2$ in the presence of DSF (Fig. S9b), the increased cellular GSH might not affect the formation of $Cu(DDC)_2$. These results indicate that the selective antitumor activity of DSF@CuPDA-PEGM highly relies on the intracellular ROS levels. The ROS-dependent antitumor effect explains why DSF@CuPDA-PEGM killed drug-resistant HCT116/L-OHP cells more effectively (Fig. 4 and Table S1), which possess higher cellular H_2O_2 than drug-sensitive HCT116 cells (Fig. S10). Therefore, in the tumor tissues or cells with high ROS contents, DSF@CuPDA-PEGM would responsively degrade for Cu^{2+} release and $Cu(DDC)_2$ synthesis in situ, resulting in precise tumor killing and minimum side effects.

The combination of DSF and Cu ions has been reported to induce cell apoptosis in a p38-dependent manner, or through the inhibition of NF-κB activity [34, 35]. In addition, copper ions could bind with lipoylated proteins in the tricarboxylic acid (TCA) cycle to induce protein oligomerization, leading to proteotoxic stress and cell cuproptosis [36]. Thus, to investigate the cell death mechanisms induced by DSF@CuPDA-PEGM, the pan-caspase inhibitor (Z-VAD-FMK) and mitochondrial electron transport chain complex I inhibitor (rotenone, a cuproptosis inhibitor) were employed. The CCK-8 assay showed that Z-VAD-FMK and rotenone markedly attenuated the cytotoxicity of DSF@CuPDA-PEGM in HCT116 cells (Fig. S11 and S12), indicating that the antitumor effect of DSF@CuPDA-PEGM is associated with both apoptosis and cuproptosis.

Cu/DSF co-treatment is able to induce immunogenic cell death (ICD) in cancer cells, with the mechanism involving the expression of damage-associated molecular pattern (DAMP) hallmarks [37]. These hallmarks include exposure of the endoplasmic reticulum protein calreticulin (CRT) and unloading of high-mobility group box 1 (HMGB1) and ATP into the extracellular space, which

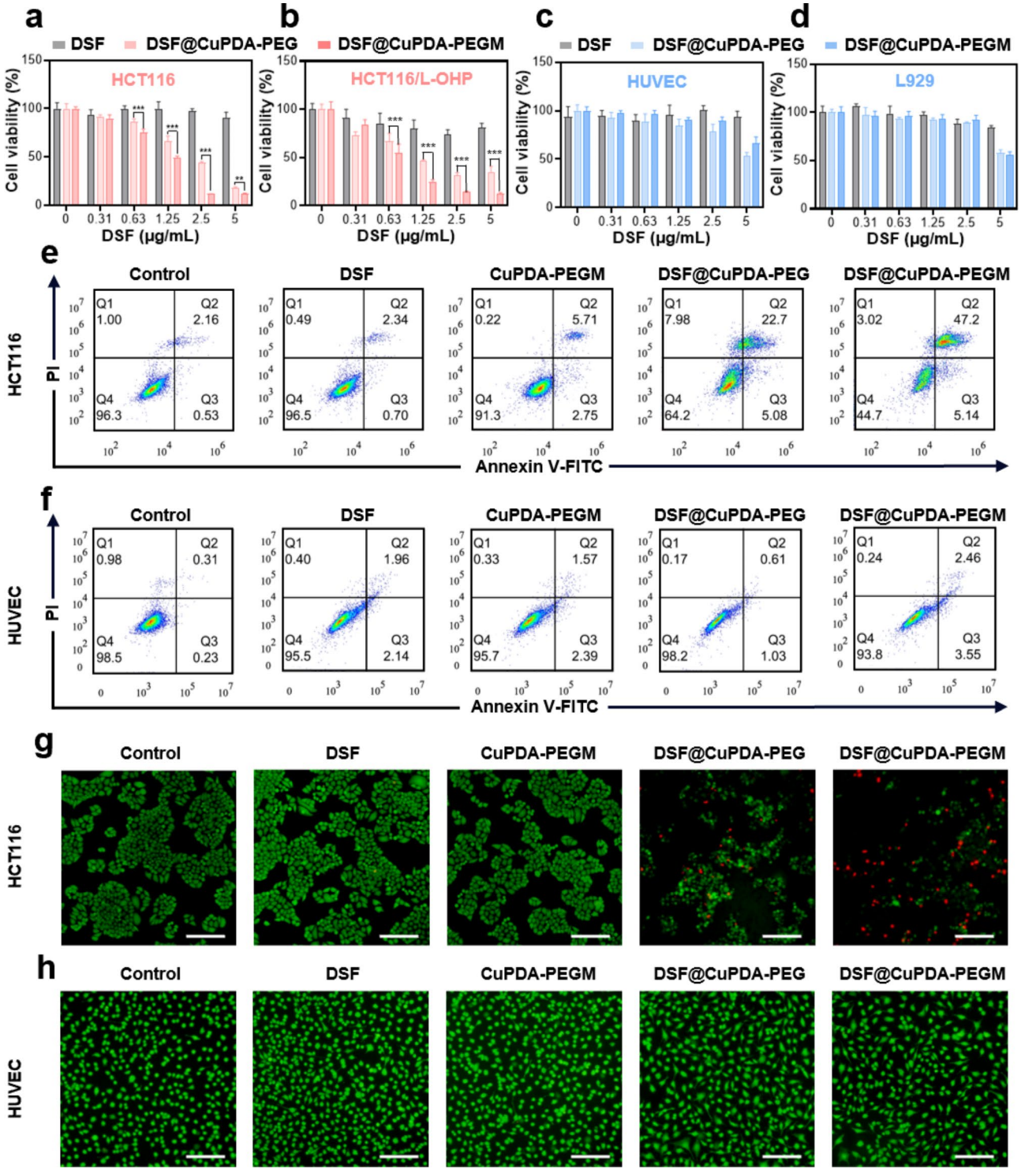

Fig. 4 Antitumor effect of DSF@CuPDA-PEGM in vitro. (**a-d**) In vitro cytotoxicity of free DSF, DSF@CuPDA-PEG, and DSF@CuPDA-PEGM against HCT116 cells (**a**), HCT116/L-OHP cells (**b**), HUVEC cells (**c**), and L929 cells (**d**) at different concentrations of DSF for 24 h. (**e-f**) Flow cytometry analysis of cell apoptosis of HCT116 cells (**e**) and HUVEC cells (**f**) receiving different treatments (DSF: 2.5 μg/mL, CuPDA-PEGM: 25 μg/mL) for 24 h. (**g-h**) Live/dead staining of HCT116 cells (**g**) and HUVEC cells (**h**) receiving different treatments (DSF: 2.5 μg/mL, CuPDA-PEGM: 25 μg/mL) for 24 h. Scale bars, 100 μm

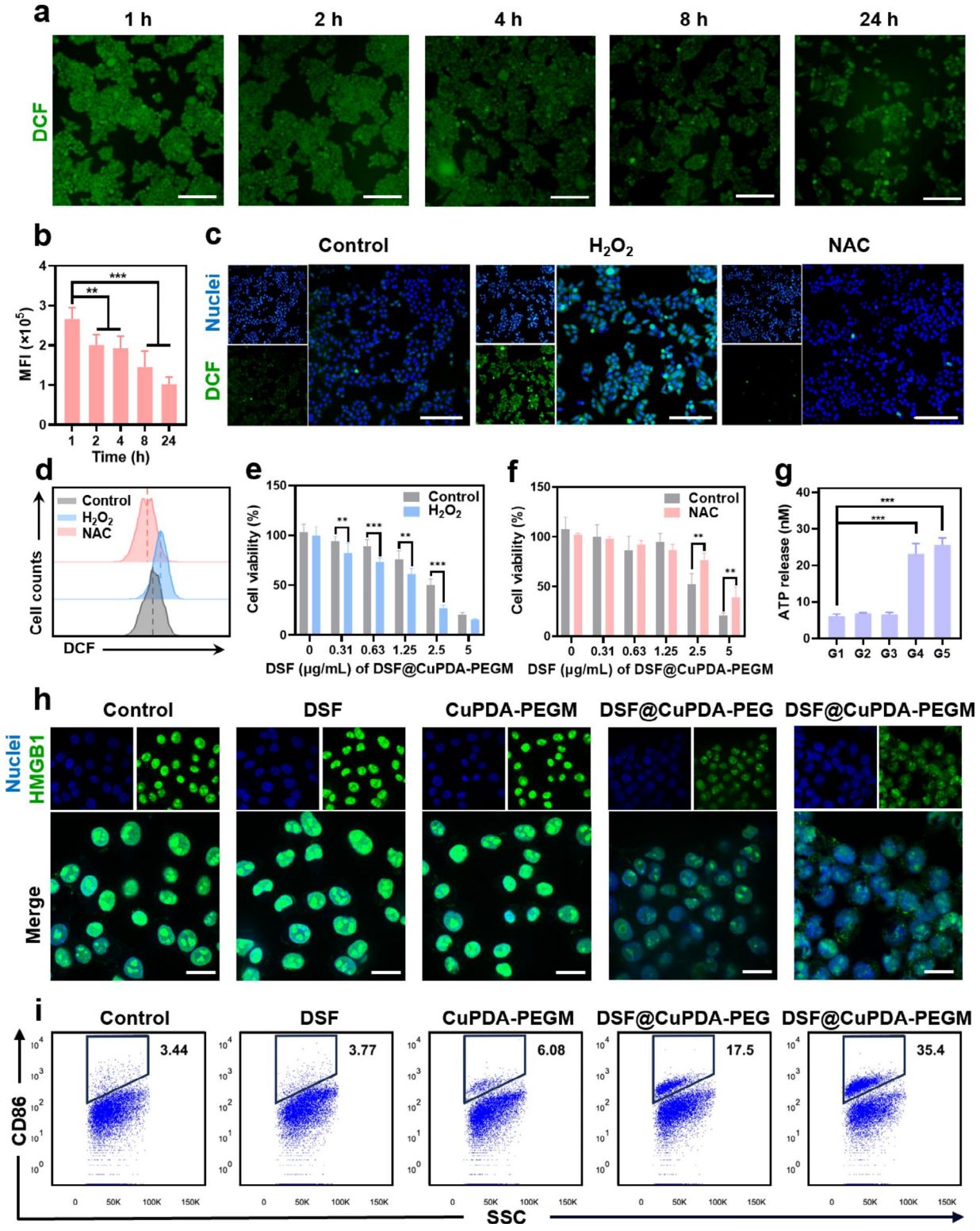

Fig. 5 The mechanisms of in vitro cell cytotoxicity and ICD effect. (**a-b**) Intracellular ROS of HCT116 cells treated with DSF@CuPDA-PEGM stained by DCFH-DA, and (**b**) quantification of mean fluorescence intensity. Scale bars, 100 μm. (**c**) Intracellular ROS levels of HCT116 cells treated with H_2O_2 or NAC. Scale bars, 100 μm. (**d**) Flow cytometry assay of intracellular ROS of HCT116 cells treated with H_2O_2 or NAC. (**e-f**) In vitro cytotoxicity of DSF@CuPDA-PEGM in the HCT116 cells, which were pretreated with H_2O_2 (**e**) or NAC (**f**). (**g**) ATP release from CT26 cells treated with PBS (G1, Control), DSF (G2), CuPDA-PEGM (G3), DSF@CuPDA-PEG (G4), DSF@CuPDA-PEGM (G5). (**h**) HMGB1 in CT26 cells after receiving different formulations. Scale bars, 20 μm. (**i**) Flow cytometry analysis of DC maturation after incubation with the cell lysates of CT26 cells which were treated with different formulations

facilitates the recruitment of dendritic cells (DCs) and promotes the antigen presentation by DCs. To study the ICD-inducing ability of DSF@CuPDA-PEGM, the ICD-related DAMPs (HMGB1 and ATP) and consequent DCs maturation were examined. DSF@CuPDA-PEG and DSF@CuPDA-PEGM effectively induced HMGB1 release, as the green fluorescence of stained HMGB1 in nuclei was markedly decreased (Fig. 5h, Fig. S13). Moreover, the ATP contents in the cell media of DSF@CuPDA-PEG and DSF@CuPDA-PEGM groups increased by 3.5 and 4.5 times, respectively (Fig. 5g), suggesting ATP secretion from the treated cells. To confirm the maturation of DCs induced by ICD, DC2.4 cells were treated with the supernatants of CT26 cells which were pre-treated with different drug formulations. Flow cytometry analysis revealed that the supernatants from cells treated with DSF-loaded nanoparticles (DSF@CuPDA-PEG and DSF@CuPDA-PEGM) effectively upregulated the DCs ($CD86^+$) maturation (Fig. 5i). Especially, the DC maturation effect of DSF@CuPDA-PEGM-treated cell medium was more effective compared with DSF@CuPDA-PEG group, likely because of the enhanced antitumor activity of DSF@CuPDA-PEGM with tumor-targeting effect. Overall, these results verified that DSF@CuPDA-PEG and DSF@CuPDA-PEGM could induce ICD in cancer cells in vitro and subsequently promote DC maturation.

In vivo antitumor effect and biocompatibility

The in vivo antitumor effect of DSF@CuPDA-PEGM was evaluated in HCT116 tumor-bearing mice (Fig. 6a). When the tumor volume reached approximately 100 mm^3, these mice were randomly divided into five groups ($n=6$) and intravenously injected with PBS, DSF, CuPDA-PEGM, DSF@CuPDA-PEG, and DSF@CuPDA-PEGM (four times, 3.75 mg/kg DSF), respectively. The DSF alone was unable to suppress tumor growth, as the tumor volume in DSF-treated mice grew as fast as the PBS group (Fig. 6b-f), indicating the low toxicity of DSF itself. Similarly, the CuPDA-PEGM (without DSF) did not inhibit the tumor growth. On the contrary, DSF-loaded CuPDA-PEGM (DSF@CuPDA-PEGM) effectively suppressed tumor growth with a tumor mass reduction of 68.4% compared with the PBS group (Fig. 6b-f). In addition, DSF@CuPDA-PEGM exhibited a significantly higher antitumor effect compared with DSF@CuPDA-PEG likely due to the targeting capability of mannose modification. Furthermore, the histochemical staining assay confirmed the antitumor effect of DSF@CuPDA-PEGM by increasing apoptotic cells (Fig. 6g). These results suggest that the combination of CuPDA-PEGM and DSF effectively inhibits tumor growth, potentially via the in situ synthesis of lethal $Cu(DDC)_2$ from DSF@CuPDA-PEGM.

Next, the biosafety of CuPDA-PEGM was evaluated in vitro and in vivo. After incubation with red blood cells for 4 h, the hemolysis rate was lower than 1% even at the concentration of 100 μg/mL, indicating good hemocompatibility of CuPDA-PEGM (Fig. S14). In addition, the viability of cells (L929, NCM460, and 3T3) exposed to CuPDA-PEGM remained higher than 80% at all the test concentrations (0–100 μg/mL), suggesting its good cytocompatibility (Fig. S15). Moreover, CuPDA-PEGM-based formulations (with or without DSF) did not decrease the body weight of mice nor damage the major organs (Fig. 6d, Fig. S16). These results suggest the favorable biocompatibility of CuPDA-PEGM. Melanin-like PDA nanoparticles are well-known for their great biocompatibility and biodegradability, making them suitable as drug delivery systems and therapeutic platforms [38]. After intravenous injection, Cu-doped PDA nanoparticles predominantly accumulate in the liver and kidneys within 24 h post-administration, attributed to the reticuloendothelial system. These nanoparticles could be completely cleared from major organs within 7 days, indicating that CuPDA could be effectively degraded and eliminated in vivo [39]. Thus, CuPDA-based nanosystems are expected to be cleared from mice and wouldn't induce long-term toxicity, owing to the biodegradability and low cytotoxicity of CuPDA (Fig. 2, S3, S15, and S16).

DSF@CuPDA-PEGM enhances the αPD-1-based tumor immunotherapy

Given the great antitumor effect and ICD-inducing capability of DSF@CuPDA-PEGM, we assumed that DSF@CuPDA-PEGM could effectively kill tumor cells to provide immunogenic signals for enhancing immunotherapy. To test this notion, we further studied the combination therapeutic efficacy of DSF@CuPDA-PEGM and immune checkpoint blockade (ICB) therapy. PD-1/PD-L1 axis causes immune evasion mediated by the mutual interaction between tumor cells and T cells or antigen-presenting cells (APCs), consequently suppressing the anti-tumor immunity of cytotoxic T lymphocytes [40, 41]. Notably, DSF/Cu^{2+} co-treatment could restrain GSK3β activity by inhibiting PARP1, leading to the upregulation of PD-L1 [42]. Hence, we evaluated the antitumor efficacy of combining DSF@CuPDA-PEGM with anti-PD-1 (αPD-1) in a microsatellite stable (MSS) CRC tumor model (CT26 tumor), which possesses a low mutational burden and poor response to ICB therapy [43, 44]. The tumor-bearing mice were treated with PBS, αPD-1, DSF@CuPDA-PEGM, and DSF@CuPDA-PEGM + αPD-1 following the schedule, respectively (Fig. 7a). The tumor volume curves and tumor weight revealed that the αPD-1 or DSF@CuPDA-PEGM alone markedly inhibited the tumor growth (about 50% reduction in the tumor mass) compared to PBS treatment (Fig. 7b-f). However, the tumor volumes of these two groups increased nearly 10 times compared with the initial tumor (Day 0), suggesting

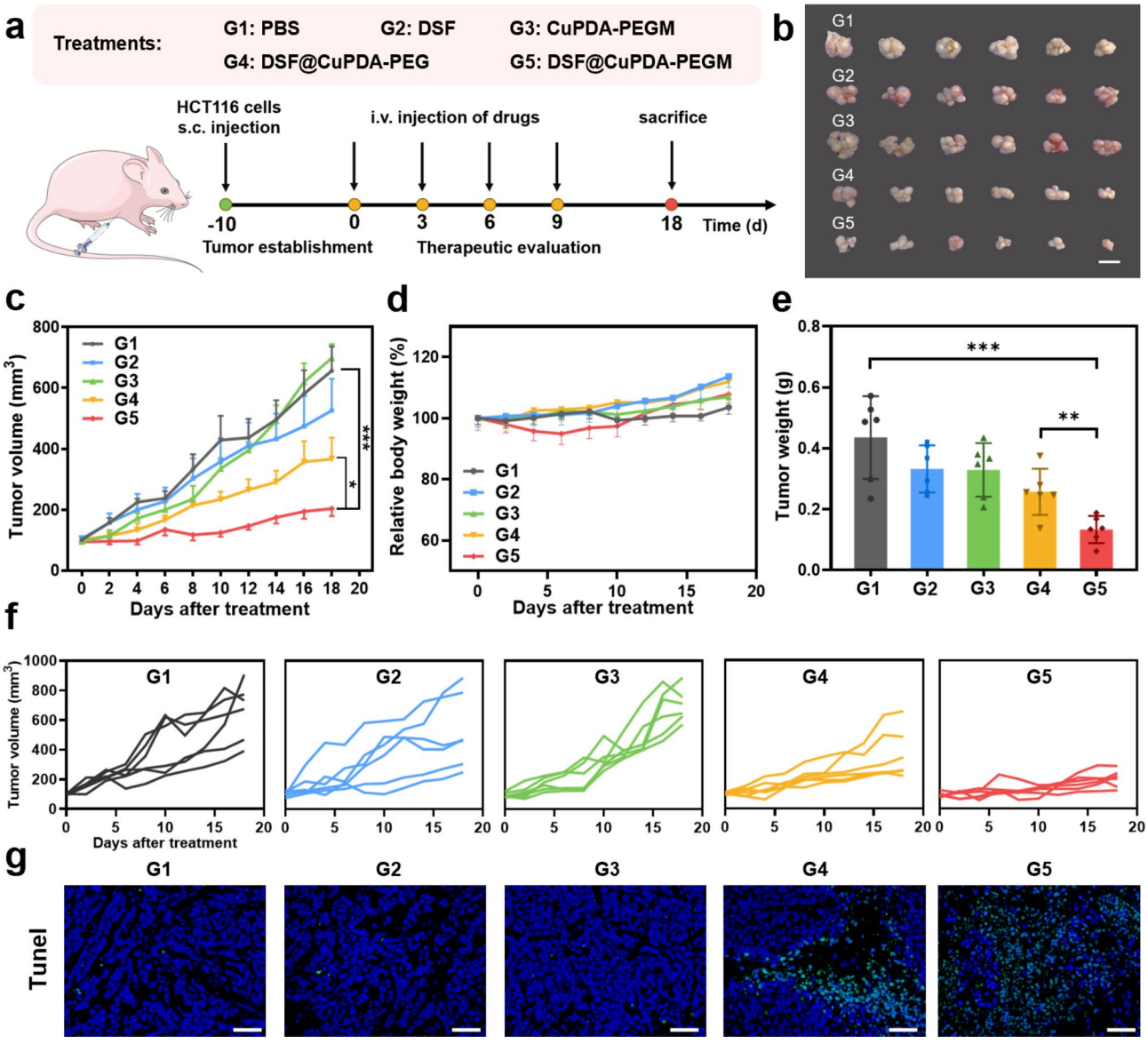

Fig. 6 In vivo antitumor effect. (**a**) Illustration of the tumor establishment and therapeutic process. HCT116 tumor-bearing nude mice were divided into 5 groups ($n=6$ per group) receiving different treatments including PBS (G1), DSF (G2), CuPDA-PEGM (G3), DSF@CuPDA-PEG (G4) and DSF@CuPDA-PEGM (G5). (**b**) Images of isolated tumors from HCT116 tumor-bearing nude mice. Scale bar, 1 cm. (**c**) Tumor-volume curves of nude mice in different groups recorded every 2 days. (**d**) The relative body weight profile of nude mice. (**e**) Tumor-weight. (**f**) Individual tumor growth profiles of tumor-bearing mice in different groups. (**g**) TUNEL staining images of tumor tissues from different groups. Scale bars, 50 μm

that the therapeutic efficacy of αPD-1 or DSF@CuPDA-PEGM is still insufficient. Remarkably, the combination of DSF@CuPDA-PEGM and αPD-1 almost completely halted the tumor growth (Fig. 7b-f). The tumor weight was reduced by 84.8% compared to the PBS group, highlighting the tumor regression efficacy of DSF@CuPDA-PEGM/αPD-1. These results confirm that DSF@CuPDA-PEGM could potentiate the immunotherapeutic effect of ICB therapy.

The antitumoral response of immunotherapy is highly reliant on the mature dendric cells (DCs), which transport tumor antigens to tumor-draining lymph nodes (TDLNs) and cross-present them to activate cytotoxic T cells [45]. To further test the antitumor immunity of the DSF@CuPDA-PEGM/αPD-1 combination, the DC maturation in TDLNs and the T cell infiltration in tumors were analyzed by flow cytometry. Notably, the combination of DSF@CuPDA-PEGM and αPD-1 induced a significant increase of mature DCs ($CD11c^+CD86^+$ DCs) in TDLNs with a level of 5.2%, markedly higher than those in PBS (3.1%, $p<0.001$), αPD-1 (3.7%, $p<0.05$), and DSF@CuPDA-PEGM groups (4.1%, $p<0.05$), indicating that αPD-1 significantly enhanced the antitumor immunity elicited by DSF@CuPDA-PEGM (Fig. 7g and h). Next, the

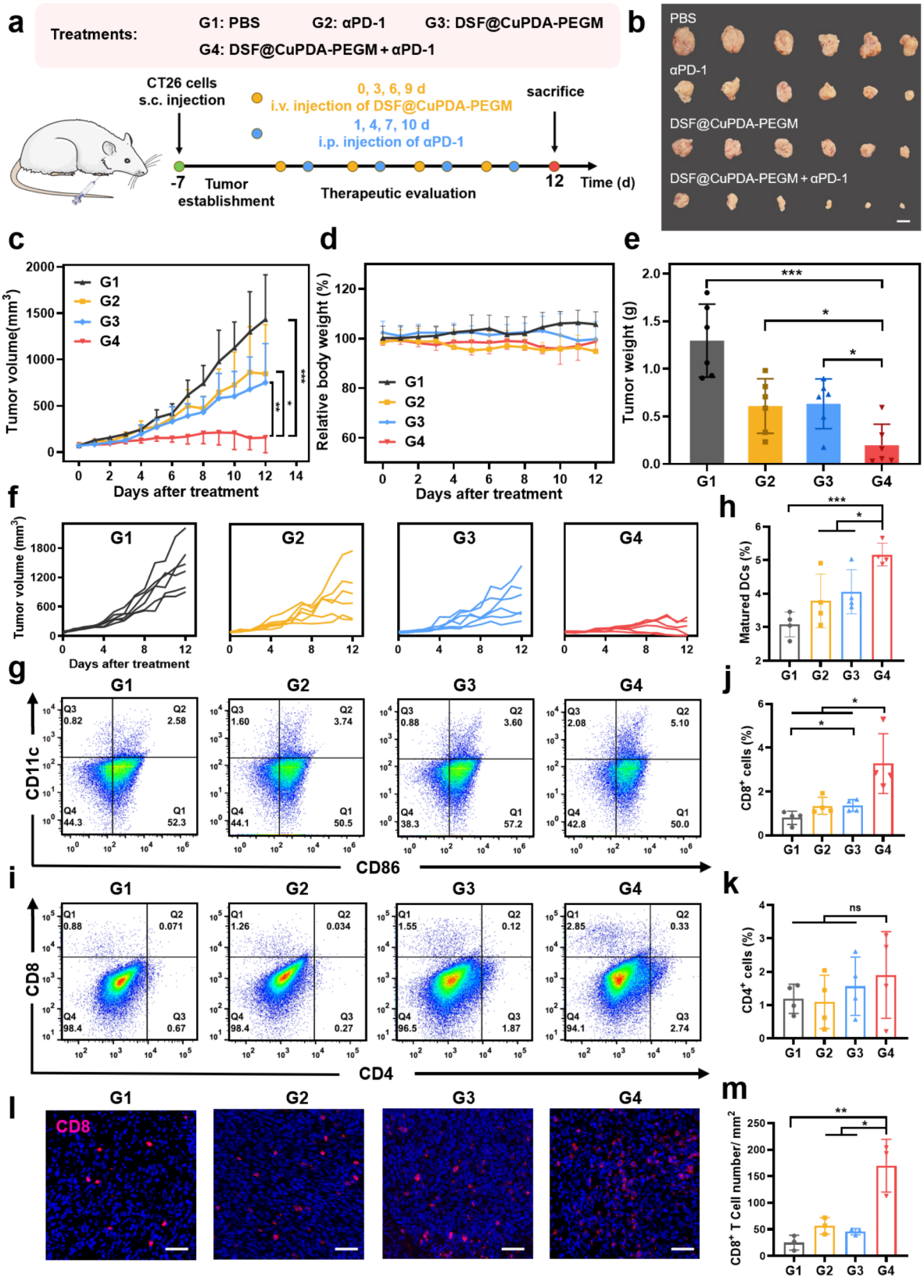

Fig. 7 (See legend on next page.)

(See figure on previous page.)

Fig. 7 Synergistic effect of DSF@CuPDA-PEGM and αPD-1 in vivo. (**a**) Schematic illustration of in vivo tumor establishment and therapeutic process. CT26 tumor-bearing BALB/c mice were divided into 4 groups ($n=6$) and treated with PBS (G1), αPD-1 (G2), DSF@CuPDA-PEGM (G3), DSF@CuPDA-PEGM plus αPD-1 (G4), respectively. (**b**) Image of tumors isolated from CT26 tumor-bearing BALB/c mice receiving treatments. Scale bar, 1 cm. (**c**) Tumor volume curves. (**d**) The relative body weight profiles of mice. (**e**) Tumor weight of the dissected tumors. (**f**) Individual tumor growth profiles ($n=6$). (**g-h**) Flow cytometric analysis of mature DCs ($CD11c^+CD86^+$) infiltration in tumor-draining lymph nodes (TDLNs) (**g**) and the quantification of mature DCs (**h**). (**i-k**) Flow cytometric analysis of T cells infiltrated in tumors ($n=4$) (**i**) and quantitative analysis of $CD8^+$ cells (**j**) and $CD4^+$ cells (**k**). (**l-m**) The immunofluorescence staining (**l**) of $CD8^+$ cells in tumors and the quantification data (**m**). Scale bars, 50 μm

T-cell infiltration in tumors was further examined by flow cytometry. Similar to the DC maturation, DSF@CuPDA-PEGM and αPD-1 synergistically promoted the infiltration of $CD8^+$ T cells in the tumor, reaching a frequency of 3.3% $CD8^+$ T cells among all the cells in the tumor, which was 2.4-fold of DSF@CuPDA-PEGM alone or αPD-1 alone (Fig. 7i and j). In addition, the immunofluorescence staining of tumor slices confirmed the distinct increase of $CD8^+$ T cell infiltration in the combination therapy group (Fig. 7l and m). However, the percentage of $CD4^+$ T cells in tumors showed no significant difference between these groups (Fig. 7i and k), possibly due to the counteractive effect of different subsets of $CD4^+$ cells. These findings collectively suggest that DSF@CuPDA-PEGM, in combination with αPD-1, can effectively enhance immune responses, demonstrating the effectiveness and versatility of DSF@CuPDA-PEGM-based chemo-immunotherapy in colorectal cancers.

Conclusion

In summary, we synthesized Cu-loaded polydopamine (CuPDA) by oxidation-polymerization and Cu-chelation, which was subsequently modified with PEG-Mannose (CuPDA-PEGM) to enhance the targeting ability towards GLUT1-overexpressed cancer cells. In the presence of high levels of H_2O_2, CuPDA was responsively degraded and released the Cu ions chelated in the nanoparticles. Therefore, DSF-loaded CuPDA-PEGM could specifically free Cu^{2+} and DSF in the cancer cells with high H_2O_2 contents, which in situ synthesized the $Cu(DDC)_2$ complex to activate the antitumor effect of DSF, enabling the effective killing of both drug-sensitive and drug-resistant cancer cells. On the contrary, in immortalized normal cells, this nanosystem exhibited significantly lower toxicity compared with cancer cells. DSF@CuPDA-PEGM monotherapy demonstrated potential antitumor efficacy in the HCT116 tumor-bearing mice. In a microsatellite stable (MSS) CT26 tumor model, DSF@CuPDA-PEGM synergized with anti-PD-1 to enhance the ICB immunotherapy via enhancing the maturation of DCs and infiltration of $CD8^+$ T cells. Thus, this study not only provides a specific and effective therapeutic nanosystem for precise tumor therapy but also offers a potent strategy to promote ICB immunotherapy. However, some challenges remain to be addressed in future studies: (1) DSF is loaded in CuPDA-PEGM via hydrophobic interactions, leading to unfavorable leakage during circulation; (2) elevated ROS levels in tissues with pathological damages, such as inflammation, might trigger the degradation of DSF@CuPDA-PEGM, potentially resulting in side effects in these regions.

Supplementary Information

The online version contains supplementary material available at https://doi.org/10.1186/s12951-024-02825-6.

Supplementary Material 1

Acknowledgements
Not applicable.

Author contributions
Z.W., L.W. and J.L. designed and supervised the research. Z.Z., C.Z., Y.Y. and M.L. performed the experiments and analyzed the data. C.Y., L.D., J.S. and Z.C. contributed to the in vivo experiments and analysis. Z.Z. and J.L. wrote the manuscript. Z.W., L.W. and J.L. revised the manuscript. All authors read and approved the final manuscript.

Funding
This work was supported by the National Natural Science Foundation of China (82072068, 82072167, 82472135, 82272277, and 82173315), Hubei Province Natural Science Foundation (2024AFA053), Major Scientific and Technological Innovation Projects of Hubei Province (2022BCA013), the Knowledge Innovation Special Project for Fundamental Research of Wuhan (2022020801010461), the Union Hospital Foundation for Young Scientist (2021xhqh01), and the Open Foundation of Hubei Key Laboratory of Regenerative Medicine and Multi-disciplinary Translational Research (2022zsyx001 and 2023zsyx012).

Data availability
No datasets were generated or analysed during the current study.

Declarations

Ethics approval and consent to participate
Animal experiments were reviewed and approved by the Animal Care and Use Committee of Huazhong University of Science and Technology (Permit Number: S2386).

Consent for publication
Not applicable.

Competing interests
The authors declare no competing interests.

Author details
[1]Research Center for Tissue Engineering and Regenerative Medicine, Union Hospital, Tongji Medical College, Huazhong University of Science and Technology, Wuhan 430022, China
[2]Department of Clinical Laboratory, Union Hospital, Tongji Medical College, Huazhong University of Science and Technology, Wuhan 430022, China
[3]Department of Gastrointestinal Surgery, Union Hospital, Tongji Medical College, Huazhong University of Science and Technology, Wuhan 430022, China

[4]Hubei Key Laboratory of Regenerative Medicine and Multi-disciplinary Translational Research, Union Hospital, Tongji Medical College, Huazhong University of Science and Technology, Wuhan 430022, China
[5]Hubei Provincial Engineering Research Center of Clinical Laboratory and Active Health Smart Equipment, Union Hospital, Tongji Medical College, Huazhong University of Science and Technology, Wuhan 430022, China

Received: 20 June 2024 / Accepted: 31 August 2024
Published online: 10 October 2024

References

1. Sung H, Ferlay J, Siegel RL, Laversanne M, Soerjomataram I, Jemal A, et al. Global Cancer statistics 2020: GLOBOCAN estimates of incidence and Mortality Worldwide for 36 cancers in 185 countries. CA Cancer J Clin. 2021;71:209–49.
2. Holohan C, Van Schaeybroeck S, Longley DB, Johnston PG. Cancer drug resistance: an evolving paradigm. Nat Rev Cancer. 2013;13:714–26.
3. Lu Y, Pan Q, Gao W, Pu Y, Luo K, He B et al. Leveraging disulfiram to treat cancer: mechanisms of action, delivery strategies, and treatment regimens. Biomaterials. 2021;121335.
4. Lewis DJ, Deshmukh P, Tedstone AA, Tuna F, O'Brien P. On the interaction of copper with disulfiram. Chem Commun. 2014;50:13334–7.
5. Skrott Z, Mistrik M, Andersen KK, Friis S, Majera D, Gursky J, et al. Alcohol-abuse drug disulfiram targets cancer via p97 segregase adaptor NPL4. Nature. 2017;552:194–9.
6. Chen H, Li X, Huo M, Wang L, Chen Y, Chen W, et al. Tumor-responsive copper-activated disulfiram for synergetic nanocatalytic tumor therapy. Nano Res. 2021;14:205–11.
7. Li B, Yao X, Li J, Lu X, Zhang W, Duan W, et al. A tumor microenvironment-activated metal-organic framework–based nanoplatform for amplified oxidative stress–induced enhanced chemotherapy. J Biol Chem. 2023;299:102742.
8. Li Q, Chao Y, Liu B, Xiao Z, Yang Z, Wu Y, et al. Disulfiram loaded calcium phosphate nanoparticles for enhanced cancer immunotherapy. Biomaterials. 2022;291:121880.
9. Wu W, Yu L, Jiang Q, Huo M, Lin H, Wang L, et al. Enhanced tumor-specific Disulfiram Chemotherapy by in situ Cu2 + chelation-initiated nontoxicity-to-toxicity transition. J Am Chem Soc. 2019;141:11531–9.
10. Wu W, Yu L, Pu Y, Yao H, Chen Y, Shi J. Copper-enriched prussian blue nanomedicine for in situ Disulfiram Toxification and Photothermal Antitumor amplification. Adv Mater. 2020;32:2000542.
11. Zhang H, Zhang Q, Guo Z, Liang K, Boyer C, Liu J, et al. Disulfiram-loaded metal organic framework for precision cancer treatment via ultrasensitive tumor microenvironment-responsive copper chelation and radical generation. J Colloid Interface Sci. 2022;615:517–26.
12. Zhang Y, Qi G, Qu X, Wang B, Ma K, Jin Y. Smart Tumor Microenvironment-Responsive Nano-Prodrug for Disulfiram Toxification in situ and the exploration of Lethal mechanisms in cells. Langmuir. 2022;38:584–92.
13. Wang C, Yang X, Dong C, Chai K, Ruan J, Shi S. Cu-related agents for cancer therapies. Coord Chem Rev. 2023;487:215156.
14. Nathan C, Cunningham-Bussel A. Beyond oxidative stress: an immunologist's guide to reactive oxygen species. Nat Rev Immunol. 2013;13:349–61.
15. Panieri E, Santoro MM. ROS homeostasis and metabolism: a dangerous liason in cancer cells. Cell Death Dis. 2016;7:e2253–2253.
16. Hayes JD, Dinkova-Kostova AT, Tew KD. Oxidative stress in Cancer. Cancer Cell. 2020;38:167–97.
17. Chen Q, Feng L, Liu J, Zhu W, Dong Z, Wu Y, et al. Intelligent Albumin–MnO_2 nanoparticles as pH-/H_2O_2-Responsive Dissociable nanocarriers to modulate Tumor Hypoxia for Effective Combination Therapy. Adv Mater. 2016;28:7129–36.
18. Cui Q, Wang JQ, Assaraf YG, Ren L, Gupta P, Wei L, et al. Modulating ROS to overcome multidrug resistance in cancer. Drug Resist Updat. 2018;41:1–25.
19. Liu J, Yuan Y, Cheng Y, Fu D, Chen Z, Wang Y, et al. Copper-based metal–Organic Framework overcomes Cancer Chemoresistance through systemically disrupting dynamically Balanced Cellular Redox Homeostasis. J Am Chem Soc. 2022;144:4799–809.
20. Zhang H, Wang T, Liu H, Han Y, Zheng Q, Xu Q, et al. Boost therapy of hepatocellular carcinoma by amplifying vicious cycle between mitochondrial oxidative stress and endoplasmic reticulum stress via biodegradable ultrasmall nanoparticles and old drug. Nano Today. 2022;46:101601.
21. Lee H, Dellatore SM, Miller WM, Messersmith PB. Mussel-inspired Surface Chemistry for Multifunctional Coatings. Science. 2007;318:426–30.
22. Liu Y, Ai K, Lu L. Polydopamine and its derivative materials: synthesis and promising applications in Energy, Environmental, and Biomedical Fields. Chem Rev. 2014;114:5057–115.
23. Bao X, Zhao J, Sun J, Hu M, Yang X. Polydopamine nanoparticles as efficient scavengers for reactive oxygen species in Periodontal Disease. ACS Nano. 2018;12:8882–92.
24. Li Y, Xie Y, Wang Z, Zang N, Carniato F, Huang Y, et al. Structure and function of Iron-loaded synthetic melanin. ACS Nano. 2016;10:10186–94.
25. Wang Z, Xie Y, Li Y, Huang Y, Parent LR, Ditri T, et al. Tunable, metal-loaded polydopamine nanoparticles analyzed by Magnetometry. Chem Mater. 2017;29:8195–201.
26. Li W, Zhou X, Liu S, Zhou J, Ding H, Gai S, et al. Biodegradable nanocatalyst with self-supplying Fenton-like ions and H2O2 for Catalytic Cascade-amplified Tumor Therapy. ACS Appl Mater Interfaces. 2021;13:50760–73.
27. Haber RS, Rathan A, Weiser KR, Pritsker A, Itzkowitz SH, Bodian C, et al. GLUT1 glucose transporter expression in colorectal carcinoma: a marker for poor prognosis. Cancer. 1998;83:34–40.
28. Yang J, Wen J, Tian T, Lu Z, Wang Y, Wang Z, et al. GLUT-1 overexpression as an unfavorable prognostic biomarker in patients with colorectal cancer. Oncotarget. 2017;8:11788–96.
29. Wu L, Jin Y, Zhao X, Tang K, Zhao Y, Tong L, et al. Tumor aerobic glycolysis confers immune evasion through modulating sensitivity to T cell-mediated bystander killing via TNF-α. Cell Metab. 2023;35:1580–96.
30. Deng X, Wang J, Yu S, Tan S, Yu T, Xu Q et al. Advances in the treatment of atherosclerosis with ligand-modified nanocarriers. Exploration. 2023;20230090.
31. Sies H, Jones DP. Reactive oxygen species (ROS) as pleiotropic physiological signalling agents. Nat Rev Mol Cell Biol. 2020;21:363–83.
32. Huang H, Zhang C, Wang X, Shao J, Chen C, Li H, et al. Overcoming hypoxia-restrained Radiotherapy using an erythrocyte-inspired and glucose-activatable platform. Nano Lett. 2020;20:4211–9.
33. Zuo H, Tao J, Shi H, He J, Zhou Z, Zhang C. Platelet-mimicking nanoparticles co-loaded with $W_{18}O_{49}$ and metformin alleviate tumor hypoxia for enhanced photodynamic therapy and photothermal therapy. Acta Biomater. 2018;80:296–307.
34. Cheriyan VT, Wang Y, Muthu M, Jamal S, Chen D, Yang H, et al. Disulfiram suppresses growth of the malignant pleural mesothelioma cells in part by inducing apoptosis. PLoS ONE. 2014;9:e93711.
35. Yip NC, Fombon IS, Liu P, Brown S, Kannappan V, Armesilla AL, et al. Disulfiram modulated ROS–MAPK and NFκB pathways and targeted breast cancer cells with cancer stem cell-like properties. Br J Cancer. 2011;104:1564–74.
36. Tsvetkov P, Coy S, Petrova B, Dreishpoon M, Verma A, Abdusamad M, et al. Copper induces cell death by targeting lipoylated TCA cycle proteins. Science. 2022;375:1254–61.
37. Sun T, Yang W, Toprani SM, Guo W, He L, DeLeo AB, et al. Induction of immunogenic cell death in radiation-resistant breast cancer stem cells by repurposing anti-alcoholism drug disulfiram. Cell Commun Signal. 2020;18:36.
38. Wang L, Song K, Jiang C, Liu S, Huang S, Yang H et al. Metal-coordinated polydopamine structures for Tumor Imaging and Therapy. Adv Healthc Mater. 2024;e2401451.
39. Xiong Y, Wang Z, Wang Q, Deng Q, Chen J, Wei J, et al. Tumor-specific activatable biopolymer nanoparticles stabilized by hydroxyethyl starch prodrug for self-amplified cooperative cancer therapy. Theranostics. 2022;12:944–62.
40. Zhang L, Gajewski TF, Kline J. PD-1/PD-L1 interactions inhibit antitumor immune responses in a murine acute myeloid leukemia model. Blood. 2009;114:1545–52.
41. Zhang C, Xia D, Liu J, Huo D, Jiang X, Hu Y. Bypassing the immunosuppression of myeloid-derived suppressor cells by reversing Tumor Hypoxia using platelet-inspired platform. Adv Funct Mater. 2020;2000189.
42. Zhou B, Guo L, Zhang B, Liu S, Zhang K, Yan J, et al. Disulfiram combined with copper induces immunosuppression via PD-L1 stabilization in hepatocellular carcinoma. Am J Cancer Res. 2019;9:2442.
43. Weng J, Li S, Zhu Z, Liu Q, Zhang R, Yang Y, et al. Exploring immunotherapy in colorectal cancer. J Hematol Oncol. 2022;15:95.

44. Li L, He S, Liao B, Wang M, Lin H, Hu B, et al. Orally Administrated Hydrogel Harnessing Intratumoral Microbiome and Microbiota-Related Immune responses for Potentiated Colorectal Cancer Treatment. Research. 2024;7:0364.
45. Gardner A, Ruffell B. Dendritic cells and Cancer Immunity. Trends Immunol. 2016;37:855–65.

Publisher's note